Final report on “Novel biophysical methods for surface-coupled antigen detection by leukocytes” OTKA PD 134195

This document summarizes our comprehensive investigation into the most suitable biophysical parameters for label-free measurement of leukocyte activation using advanced biophysical platforms. Our objective was to identify methodologies that provide detailed, scalable, and reproducible data on cell activation, particularly at the single-cell level.

The question of how individual cells function differently in response to various triggers and perturbations necessitates methods that can characterize cellular heterogeneity with single-cell resolution. Traditionally, most cell analysis techniques measured bulk responses, failing to account for smaller subpopulations within mixtures and overlooking differences between individual cells (Altschuler and Wu, 2010). This limitation has hindered our understanding of the complexity of cellular functions, particularly within the immune system.

Recent advancements in single-cell analysis technologies have provided an unprecedented level of detail, allowing researchers to explore cellular heterogeneity with greater precision. These advancements offer new insights into how different cell types respond to stimuli and interact within the immune system. However, these techniques often rely on the expression of predefined molecular markers, creating a complex system with numerous variables. Interpreting these results can be challenging due to the intricate interplay between these molecules.

In immune research, the relevance of single-cell analysis is indisputable. Current approaches, such as labeling-based phenotyping, provide valuable insights into cell types and their distributions. However, these methods fall short in capturing the full functional complexity of immune cells. For instance, phenotypic analysis does not fully address functional cell states or their variations at the single-cell level (Satija and Shalek, 2014).

Many existing techniques for characterizing immune cell heterogeneity rely on established cell lines, such as THP-1 for antibody-dependent cellular phagocytosis (ADCP), or on cells isolated from unrelated healthy donors to assess processes like antibody-dependent neutrophil phagocytosis (ADNP) and NK-cell activation assays. While useful, these models fail to account for allotypic variations in antibodies and their Fc receptors, ignoring inter-individual differences that may lead to biased results. This limitation underscores the need for more comprehensive methods that accurately reflect the diversity of the immune cells’ functional states in response to antibodies and their complexes (Lu et al., 2018).

The complete characterization of a vaccine’s efficacy, for example, requires multiplexed testing involving multiple reagents and steps, with each test conducted separately(Loos et al., 2023). This complexity likely increases the likelihood of inconsistencies, making it difficult to generate a coherent and unbiased immune profile. Furthermore, most current assays for assessing immune cell effector functions lack the single-cell resolution necessary to capture the full range of cellular behavior (Lodge et al., 2025).

To address these challenges, novel approaches to characterizing cellular heterogeneity are being explored. One promising direction is the characterization of net functional outcomes, providing a more holistic view of immune cell functionality. This approach allows researchers to describe cellular heterogeneity without relying on predefined markers or labels, offering a more unbiased perspective on immune system function. In summary, single-cell resolution is crucial for accurate immune profiling. Current methods face limitations in capturing the full complexity of immune cell functions and interactions. To advance our understanding of cellular behavior, new technologies must provide label-free, single-cell resolution, enabling more precise and unbiased characterization of immune cells and their functional states.

Label-free optical biosensors and biophysical measurement platforms present a novel opportunity to characterize single-cell parameters, such as adhesion strength, activation kinetics (based on changes

in the local refractive index), and morphological changes in individual cells. These innovative approaches have the potential to revolutionize immune profiling, offering deeper insights into cellular heterogeneity and function(Szittner et al., 2022).

To address this, we adopted a stepwise approach, beginning with the activation of THP-1 cells on immunoglobulin-coated surfaces. This was later extended to leukocytes activated on various immune complexes and in the presence of Toll-like receptor (TLR) ligands. The comparative evaluation of biophysical techniques to evaluate key parameters of leukocyte behavior during activation, potentially paves the way for leukocyte based immune profiling. This report details our findings, challenges encountered, and future directions for the application and refinement of the following parameters:

Relative Adhesion Force: We compared a computer-controlled micropipette and FluidFM system to measure the adhesion strength of single cells, providing insight into the mechanical changes occurring during immunoglobulin triggered activation.
Morphology and Motility: Cell shape and movement were analyzed using digital holographic microscope, Holomonitor, a quantitative phase imaging platform that allowed real-time, non-invasive visualization of dynamic changes.
Activation Kinetics: Using a resonant waveguide grating (RWG)-based biosensor, we monitored the kinetics of cell activation, focusing on real-time detection of biophysical changes at the single-cell level.

Single cell adhesion force

Two methods Fluidic Force Microscopy (FluidFM) and Computer Controlled Micropipette (CCMP were used to test the relative force required to detach cells form the immunoglobulin functionalized surface, and to reveal the distribution of the cell adhesion strength values on single cells. After setting up the parameters and buffer requirements of the measurement were compared with the classic negative pressure based CCMP results and the FluidFM. We found that cells specifically adhere to the immunoglobulins on the surface, as if no immunoglobulins were present no cell adhesion was measurable, when the surface was blocked. Since with FluidFM

We proved that the measurement is able to characterize the relative forces. While, the two tested methods showed comparable relative adhesion force, the distribution scattered widely. compared to other methods their throughput (cells measured per hour) is relatively low compared to other methods, moreover provides only single end-point measurement results. As will be discussed later on in detail a likely reason behind the wide range of values, is the dynamic manner of cell adhesion during the activation process. On the other hand, as we successfully demonstrated the CCMP method is readily available to transfer single cells with a high precision to specific locations and containers.

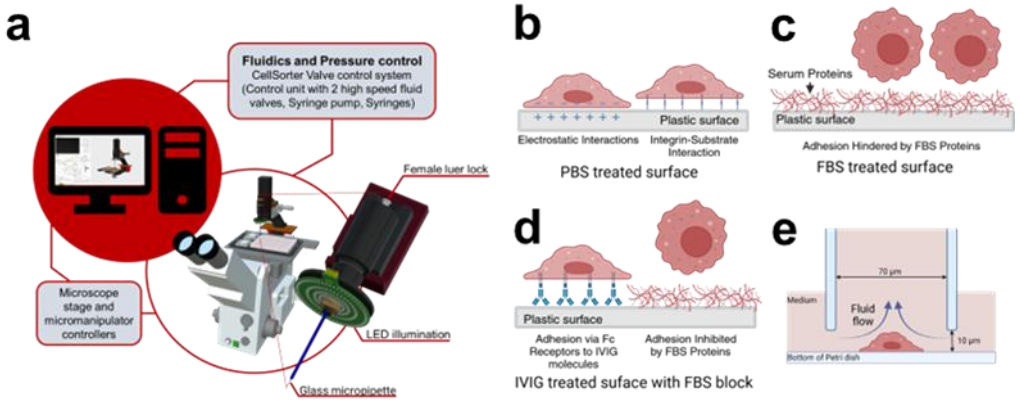

Figure 1. Schematics of the computer-controlled micropipette and the theoretical basis of the experiments. a *Cell sorting equipment for automated sorting and deposition of individual cells* ***b-d***

images show how different surface treatments affect the interaction between the cells and the surface ***b*** *Cells may adhere on an untreated surface in Phosphate Buffered Saline (PBS) in a non-specific manner triggered by electrostatic interactions or in an integrin mediated manner.* ***c*** *Fetal Bovine Serum (FBS) treatment prevents adhesion to the surface* ***d*** *FBS block applied after Intravenous Immunoglobulin (IVIG) surface treatment prevents non-specific adhesion of the cells to the surface, only Fc receptor-specific binding occurs* ***e*** *Shows the concept of cell adhesion measurement.*

To demonstrate our ability to measure the strength of specific binding between the Fc receptors of THP-1 cells and Intravenous Immunoglobulin (IVIG) molecules, we measured the relative cell binding strength on different surfaces using CCMP (Fig1). Both conventional and Tissue culture Petri dishes were used to perform surface treatments (Fig2A-B). Both bar graph shows the percentage of cells remaining attached to the surface after passing over them with a given vacuum and shows three different treatments next to each other represented by a different color bar. When RF was applied alone it shows that the FBS in the RF solution completely blocked the surface, and the cells were unable to attach. When we used this in combination with IVIG surface treatment however, only adhesions specific to IVIG stayed on the Petri dish's surface because the FBS blocked the nonspecific binding points that IVIG couldn't coat. The PBS-treated surface was used as a control as the cells were attached to the surface by several methods like electrostatic and integrin-substrate interaction. The number of cells remaining adherent shows a significant difference between treatments, especially at the initial vacuum values.

We looked at the reproducibility of experiments within and between petri dishes (Fig2E). For the measurements, we used IVIG on a treated surface, tested two areas per petri dish and found that there was minimal disparity when working with a sufficiently large number of cells.

We used ReadyProbes® Cell Viability Imaging Kit during some measurements to ensure that the cell population is in the right condition for the experiment So we test whether cell death could affect the adhesion measurements and the average number of dead cells that could occur in a series (Fig2D).

In order to speed up the experimental work and reduce the resulting scatter, different variables were compared to see how they influence the change in cell adhesion. To scale down the experiment to reduce the material dependence, measurements were made on 96-well plates instead of Petri dishes (Fig2C), but these significantly reduced the adhesion at higher vacuum values. Since BSA is a more purified version of the FBS solution, the possibility arose that it might have a different effect on the adhesion ability of the cells, so the two blocking methods were compared but there was no significant difference (Fig2F).

Surface treatment is time-consuming and stretches the preparation time before the measurement, so we looked at whether preparing it the day before would cause a change in adhesion, because it would have helped in speeding up the work (Fig2G). We are most interested in the initial vacuum values in these measurements as this was the most significant difference between the surface treatments and we saw no significant variance.

Isolation and preparation of the cells can also affect their adhesivity, so we compared how changing the measuring medium in which the cells adhere to the IVIG molecule. We looked at the difference in cell adherence to the surface between PBS and RF solution or the solvent in which the cells are resuspended after isolation might change the adhesion of the cells, but we found no significant change(Fig2H-I).

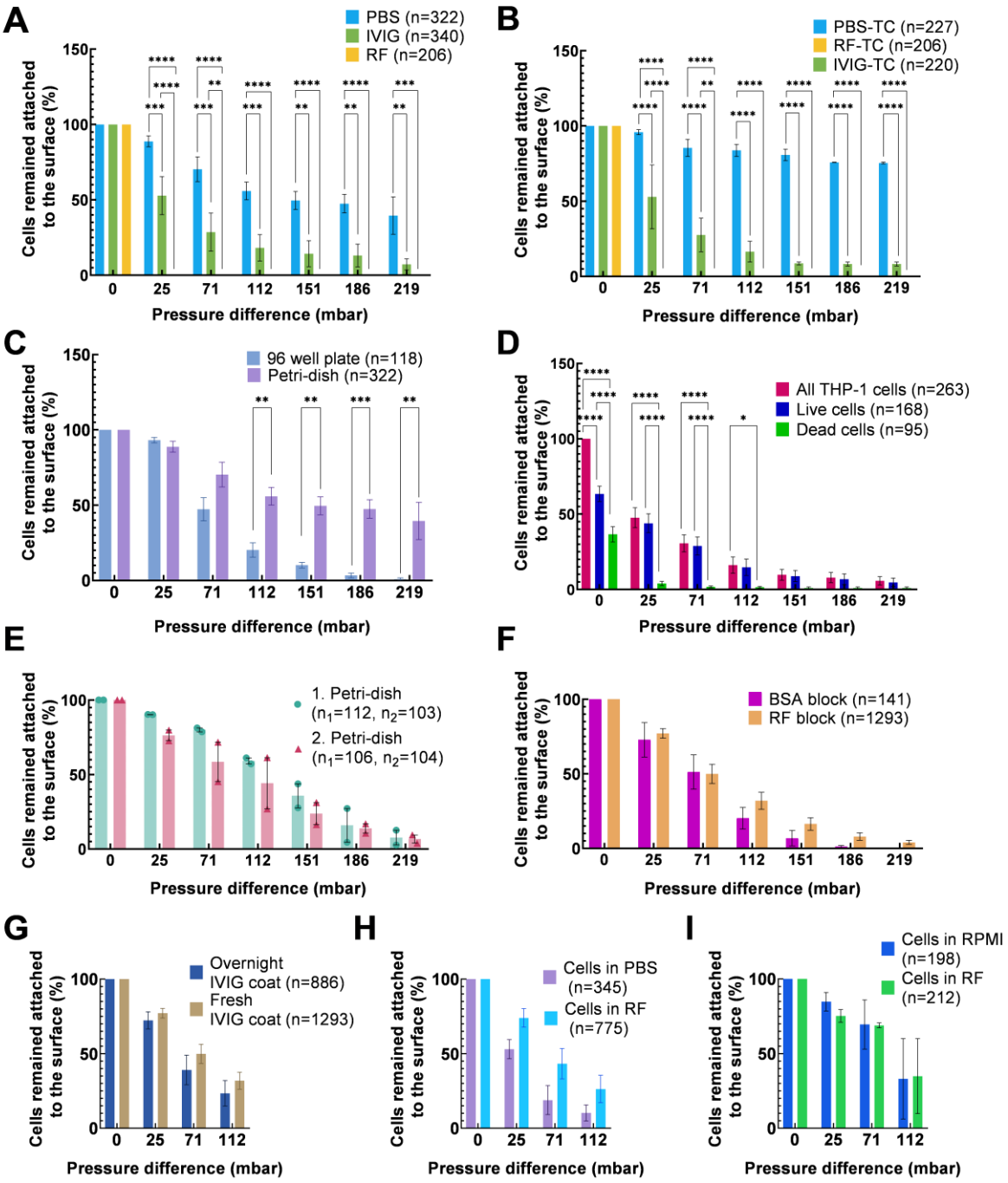

Figure 2. Parameters of immunoglobulin triggered cell adhesion measurements with CCMP. ***A*** *Percentage of cells remained attached to the surface of regular Petri-dishes with different surface treatments at increasing negative pressure values. Intravenous Immunoglobulin (IVIG) treated surfaces were also blocked with RPMI + 10% (Fetal Bovine Serum) FBS (RF).* ***B*** *Cells remained attached to the surface of Tissue culture Petri-dishes with different surface treatments.* ***C*** *Comparison of cell adhesion strength on IVIG on Petri dish and 96 well plate surface.* ***D*** *Comparison of the adhesion ability of living and dead cells using viability assay on IVIG.* ***E*** *Shows how closely a measurement in a given Petri dish compares with a measurement in another area, and between two different IVIG coated Petri-dishes.* ***F*** *Difference in cell adhesion ability with either RF or BSA surface blocking after IVIG surface treatment.* ***G*** *Difference in cell adhesion ability depending on whether the IVIG surface treatment was prepared before the experiments or the day before.* ***H*** *Difference in cell adhesion ability between cells resuspended in either RF or PBS.* ***I*** *Difference in the adhesion of cells depending on whether the cells are in empty*

*RPMI solution or in RF solution during the measurement. Data is shown as the mean ± SEM of multiple measurements. During the statistical analysis, a two-way ANOVA test was conducted with either Turkey or Bonferroni comparison test, the significance levels for statistical analysis were denoted as follows: * for p ≤ 0.05, ** for p≤0.01, *** for p≤0.001, and **** for p≤0.0001., statistically non-significant results are not marked, n indicates how many individual cells were measured in total for a given set of parameters.*

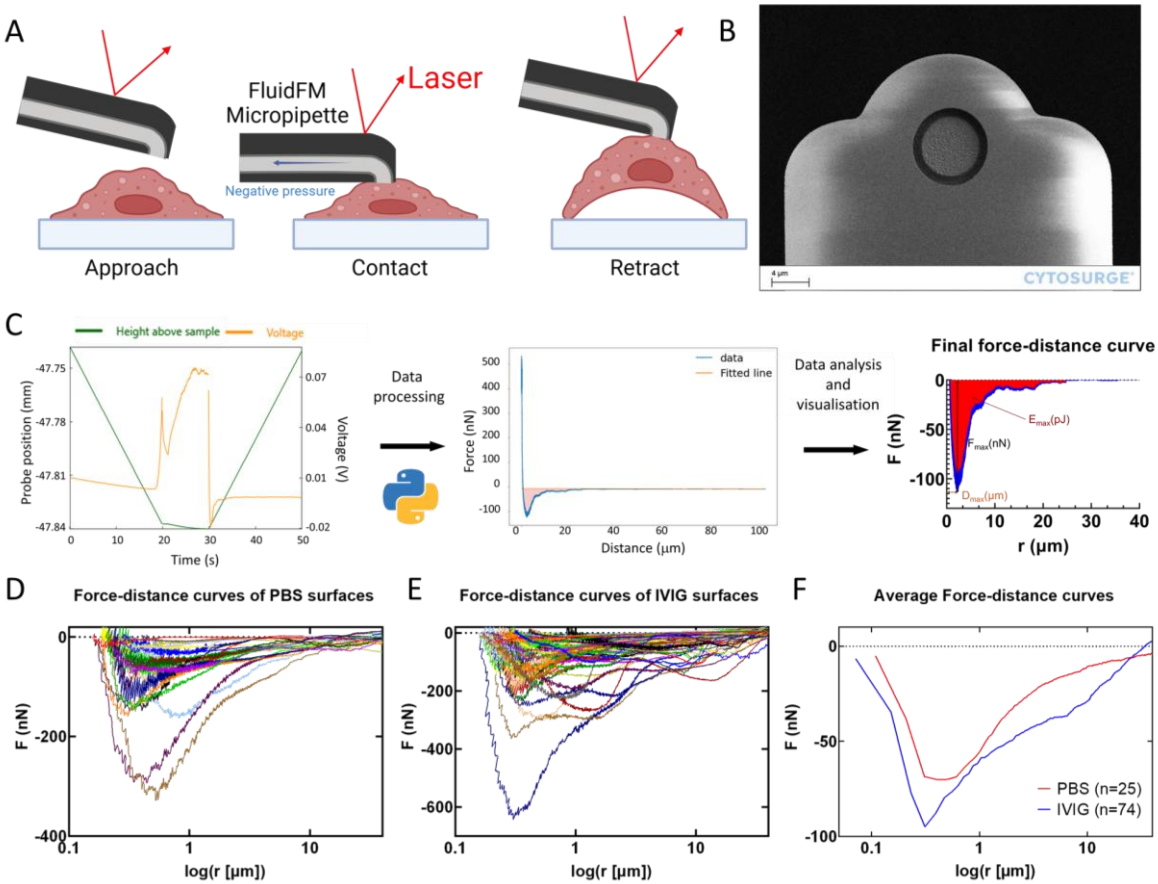

Figure 3. The working principle of the FluidFM and processing of the gathered data. ***A*** *The process of measuring cell adhesion with FluidFM* ***B*** *An electron microscope image of a cantilever used in an experiment (www.cytosurge.com).* ***C*** *The FluidFM data processing pipeline and the values provided by a single measurement. Here E_{max} shows the total adhesion energy, F_{max} the maximum adhesion strength and D_{max} shows the probe distance from the surface at F_{max} obtained during the measurement of a single cell.* ***D*** *The processed force-distance curves of PBS treated surfaces and* ***E*** *IVIG treated surfaces.* ***F*** *The averaged force distance curves of both surfaces. Data is presented on logarithmic scale to make individual differences more apparent.*

Since the CCMP only provides indirect information on the strength and characteristics of adhesion we employed a FluidFM system that could measure each adhered cell's force curve as it separated from the surface. The principle of the single cell measurements can be seen on Figure 3A, while Figure 3B shows the electron microscope image of a cantilever. The measurements were performed only on IVIG treated and RF blocked, and plain PBS treated surfaces since it is not possible to measure adhesion on non-adherent cells in only RF treated areas. We successfully measured the adhesion data of 25 cells on PBS and 75 cells on IVIG treated surface. The raw data given by the equipment software was then processed using an internally developed python code schematically represent on Figure 3C. This made the task faster and more manageable and so we could extract the Force-distance curves of the individual cells with ease. Figure 4D-E shows the individual cells curves while Figure 4F plots the averages side

by side. It is not possible to give an accurate opinion on these curves alone, so pure values must be obtained. These vales that we can extract from these curves are the adhesion force, distance, and energy (Figure 4C). The adhesion force is the maximum force that which the adherent cell can bend the cantilever before separating from the surface. The adhesion distance is the point where the cell exerts the greatest force on the continuously rising spring plate before breaking away from the surface and the adhesion energy is the area under the force-distance curve it gives how much energy was needed for the cantilever to retreat to a neutral state from attachment.

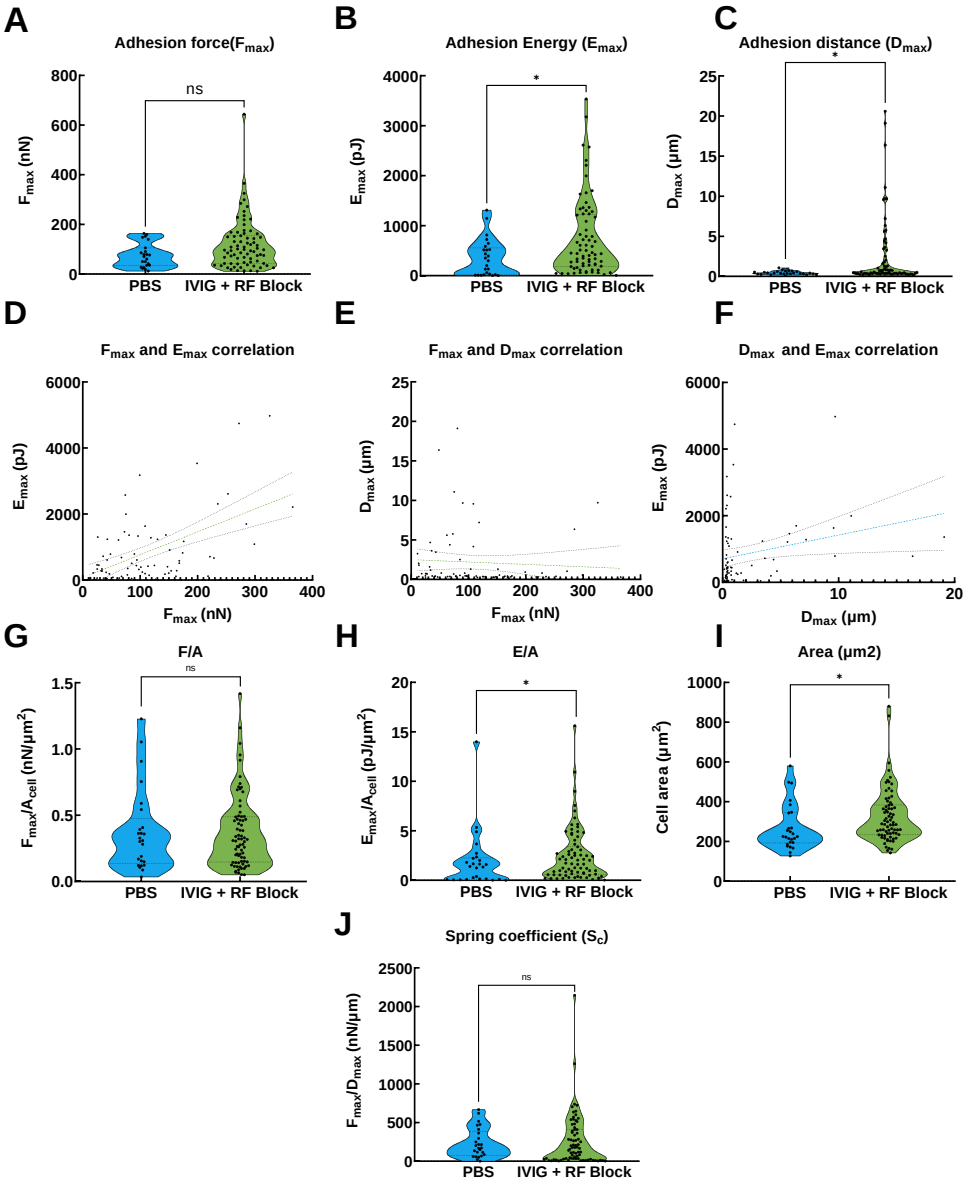

Figure 4. Comparison of biophysical parameters of single cell adhesion on PBS and IVIG treated surfaces by fluidic force microscopy. *Comparison of **A** adhesion force, **B** adhesion energy and **C** adhesion distance on PBS and IVIG treated surfaces. Correlation between **D** adhesion force and energy **E** adhesion force and distance and **F** adhesion distance and energy on IVIG treated surface. Comparison of **G** Adhesion force normalized with area, **H** Adhesion energy normalized with area and **I** cell area on PBS and IVIG treated surfaces. **J** Comparison of Spring coefficient on PBS and IVIG treated surfaces. The data are represented by individual data points and the statistical analysis was an unpaired non-parametric t test (Mann-Whitney test) the significance levels for statistical analysis were denoted as follows: * for p ≤ 0.05, ** for p≤0.01, *** for p≤0.001, and **** for p≤0.0001.*

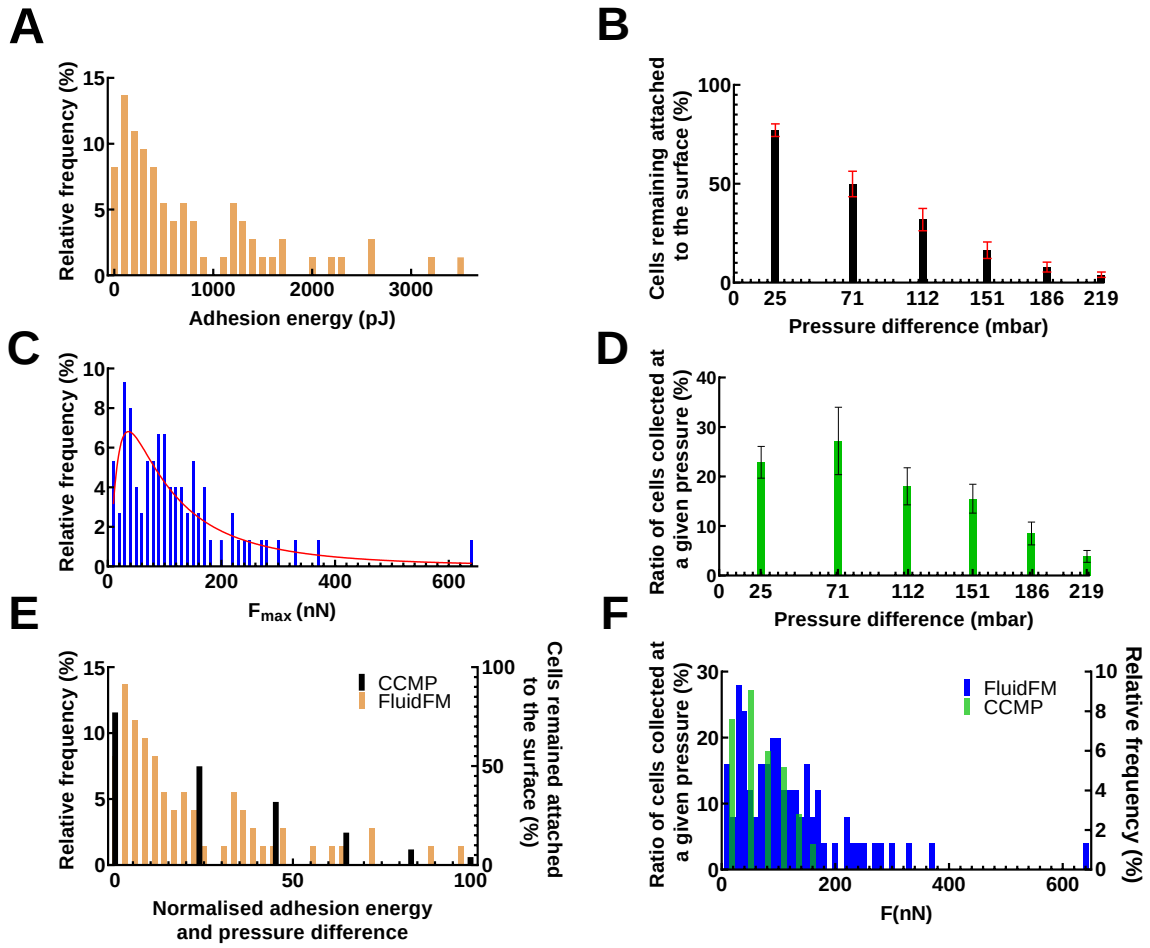

Figure 5. Comparison of the FluidFM and the CCMP results. A *Relative frequency distribution of single cell the adhesion energy on IVIG treated surfaces measured by FluidFM.* ***B*** *Normalized percentage of single cells remaining attached to the IVIG treated surfaces with the CCMP.* ***C*** *Relative frequency distribution of single cell the adhesion force of cells on IVIG treated surfaces measured by FluidFM.* ***D*** *Ratio of cells that were detached from the IVIG treated surface during CCMP measurements.* ***E*** *Comparison of the frequency of adhesion energy and the ratio of cells stayed adhered to the IVIG surface.* ***F*** *Comparison of the converted CCMP measurements to the adhesion force of the FluidFM measurements.*

A comparison of these values between the two surfaces shows that there is a significant difference in distance and energy between the cell adhesion caused in favor of the IVIG treated surface seen on Figure 4A-C. On the IVIG treated surface we also looked at how the obtained values correlate of the and here we can see that there is only a weak positive correlation between the force and the energy (Figure 4D) while there was no correlation between the distance and the energy (Figure 4F) and between the force and distance there is no correlation (Figure 4E). As the adhesion is caused by the interaction between Fc receptors and IgG antibodies, we can't expect a strong correlation since the strength of the adhesion is highly dependent on how many receptors can each cell utilize. On the treated surface localized low- and high-density ligand spot can cause further disruptions.

The cell area was determined and compared between the two surfaces and as we anticipated the cells spread out more during frustrated phagocytosis (Figure 4I). We also compared the force and energy normalized by the cell area and only found differences between the two surfaces only in adhesion energy (Figure 5G-H). We also determined and compared the spring coefficient of the cells on the different

surfaces and found no difference (Figure 5J). Since this value tells information about average elasticity of the cells we expected this to be similar considering we used identical cells.

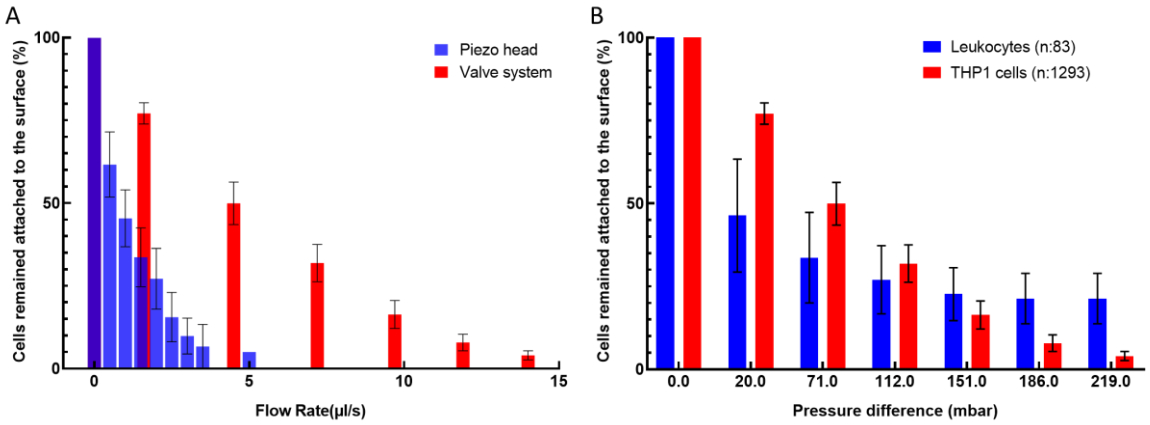

Figure 6. ***A*** *Comparison relative frequency distribution of single cell the adhesion energy on IVIG treated surfaces measured by Piezoelectric volume control system and valve control system.* ***B*** *Comparison of normalized percentage of single THP-1 cells and leukocytes remaining attached to the IVIG treated surfaces with the CCMP valve system.*

We also tested the piezoelectric valve system and compared our results to the classic negative pressure based valve system (Fig6A). Comparing the two methods, it can be seen that the piezoelectric system exerts less force on the cells due to the different operation, so the adhesion curve is much less elongated although its characteristic is similar. One reason can be that during the Piezo measurements the duration in which the voltage was applied was 100ms while during Valve measurements (Quickpick) the valve was open for 25ms during which the valve system provides a constant pressure during this time the piezo system distributes the created vacuum at the given time.

Utilizing voltage modifications, this cutting-edge apparatus excels at producing adjustments in minuscule volumes. The newly employed instrument consistently produced similar results on both treated and untreated surfaces, thereby reinforcing the findings of previous experiments. Afterwards, we measured peripheral blood derived human leukocytes as well. A comparison analysis was performed to assess the adhesion qualities of white blood cells and THP-1 cells in these first assessments. It was observed that activated cells, most likely neutrophils, showed increased persistent adhesion to surfaces covered with IVIG (Fig6B).

Both techniques are capable of measuring cell adhesion, but only FluidFM provides direct force measurements. However, the throughput of FluidFM is significantly lower than that of CCMP. By combining the two techniques, we can more rapidly gather adhesion data across various surface treatments: CCMP allows for quick screening and selection of relevant adhesion interactions across a series of experiments, after which precise force measurements can be obtained using FluidFM. The preparation of this manuscript is in its final phase. Of note we found the CCMP technology really useful in micromanipulation, selection and precise handling of single cells as presented in our recent publication (Bányász et al., 2023).

Single cell morphology and motility

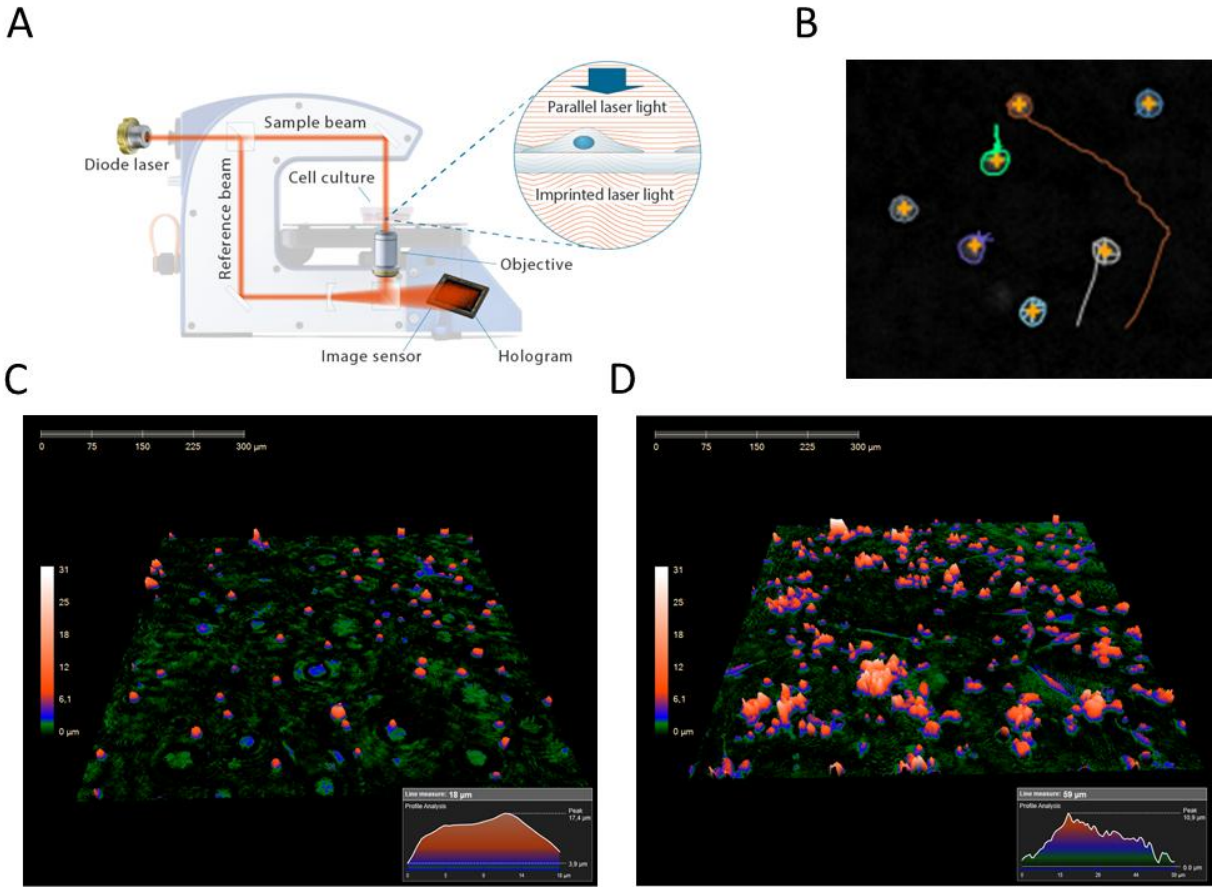

Figure 7. Schematic overview of the Holomonitor platform*. **A** In the instrument, a beam splitter divides the 635 nm laser beam from the laser diode into two directions: one is the reference beam, and the other is the sample beam. The laser beam passing through the sample undergoes a phase shift. The interference pattern created by the two incoming laser beams forms the hologram, which is detected by a digital sensor. The software then numerically reconstructs and displays the image. (source: https://phiab.com/wp-content/uploads/2019/07/Holographic-microscopy-principle.png) **B** Shows the principle of the evaluation of the image output, here single cells are located in each frame throughput the measurement to follow changes in their morphological parameters and movement. **C** and **D** Shows the region of interest with the cells at the beginning (**C**) and after 96 hours of incubation (**D**), on IVIG coated surface in the presence of soluble peptidoglycan.*

Holomonitor, a quantitative phase contrast microscopy platform (Fig7A), was used to test morphological parameters of THP-1 cell activation and movement of single cells to further characterize their activation. Using the same setup as in case of adhesion force measurements we investigated the cell activation on IVIG coating with various blocking agents and surfaces(Fig9). Here the data evaluation is based on algorithm assisted image analysis, however recognition of each cell is to be adjusted manually through all recorded frames that are to be evaluated (Fig7B). This notion likely introduces biased evaluation, moreover, fine structures of the cells are fading into the background noise in most cases. With this platform, cell area and irregularity, optical thickness and motility proved to be useful parameters to describe the frustrated phagocytosis of THP-1 cells on IVIG coated surfaces (Fig8). In general, IVIG activated cells flatten, their area increases, the move less and tend to have more protrusions, resulting higher shape irregularity. This activation can be inhibited with IVIG added in solution (Fig9D).

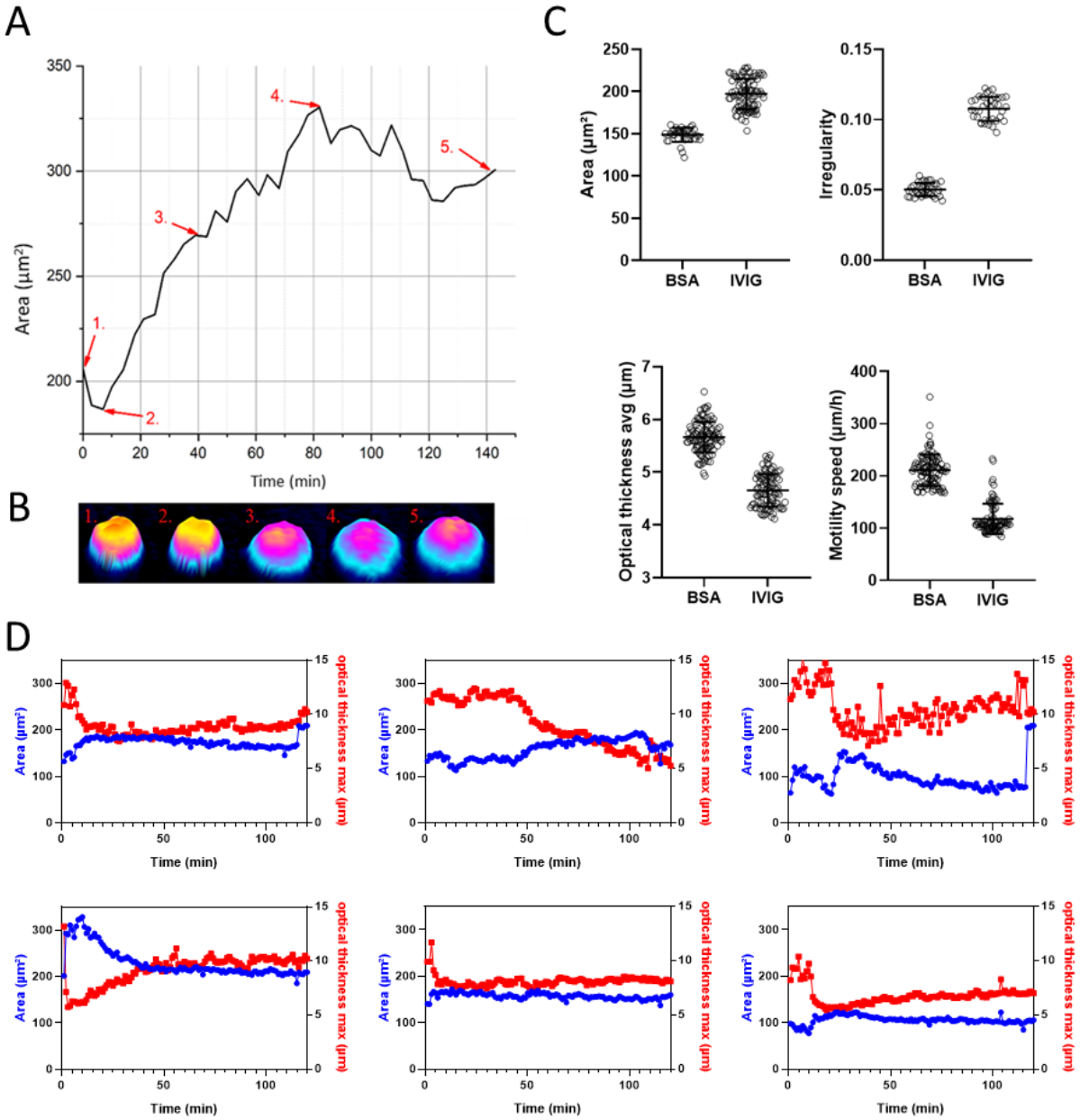

Figure 8. THP-1 cell activation characteristics in the Holomonitor. ***A*** *Cell spreading on IVIG coated surfaces blocked by RF and* ***B*** *Holographic reconstruction of the cell shown in* ***(A)****.* ***C*** *Distribution area, irregularity, average optical thickness and motility speed on BSA and IVIG coated surfaces at the end of a 2-hour measurement, while* ***D*** *shows the interaction of area and maximal optical thickness in case of single cells.*

While Holomonitor offers multi-well measurements by its motorized and programmable sample stage, and thus in principle a high throughput measurement, the stage movement and refocusing takes too long and it's a great disadvantage of the system. For example, a theoretically 1-hour measurement, taking 1 picture per minute in 16 wells, takes approximately 3 and a half hours. This time resolution is well below the that of the later introduced RWG based systems for multi-well measurements. Therefore, with this current setup only a few wells should be measured simultaneously. Also since cells in may start to activate as soon as they land on the immunoglobulin treated surface, in many case only a glimpse can

be recorded of the activation process (Fig8D). IVIG functionalized polyacrylamide and carboxymethyl-dextran based surfaces were also tested and showed comparable results to regular surfaces (Fig9A-B). The greatest advantage of this platform is that it's completely incubator proof therefore long-term measurements even of weeks can be performed to follow single cell differentiation on real time (Fig7C-D; Fig9).

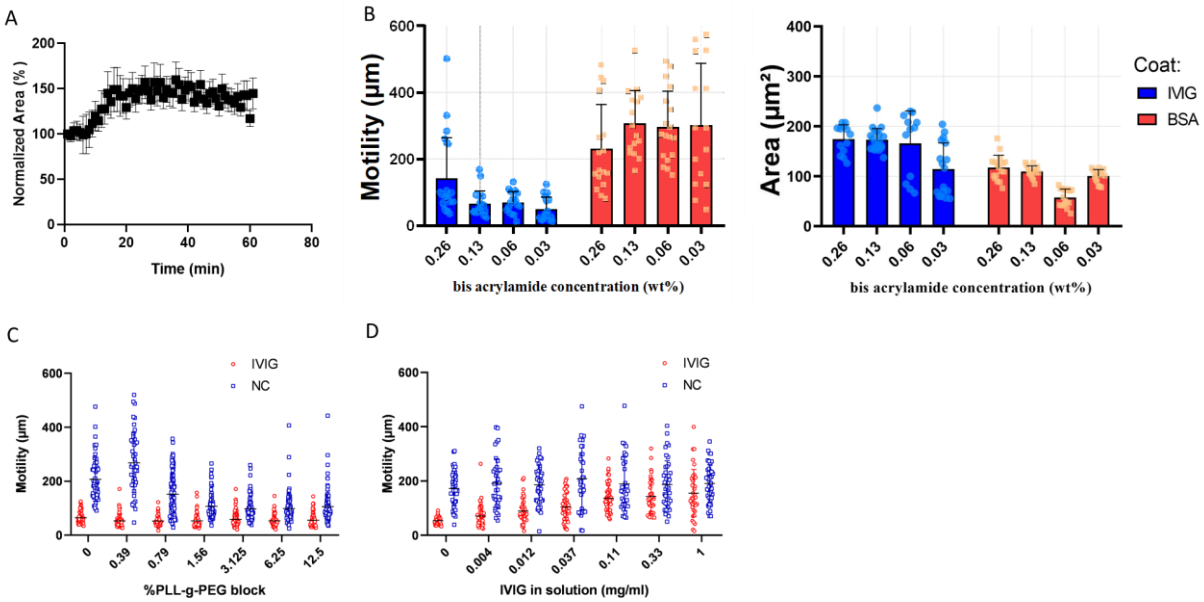

Figure 9. THP-1 cell activation characteristics in the Holomonitor on various surfaces. ***A*** *Shows normalized cell area on IVIG functionalized carboxymethyl-dextran surfaces.* ***B*** *Motility and area of single cells on IVIG and BSA functionalized polyacrylamide surface.* ***C*** *The effect of poly(L-lysine) - graft-poly(ethylene glycol) (PLL-g-PEG) blocking on cell motility on IVIG coated and non-coated surfaces.* ***D*** *The effect of soluble IVIG on the motility of cells. Markers represent single cells.*

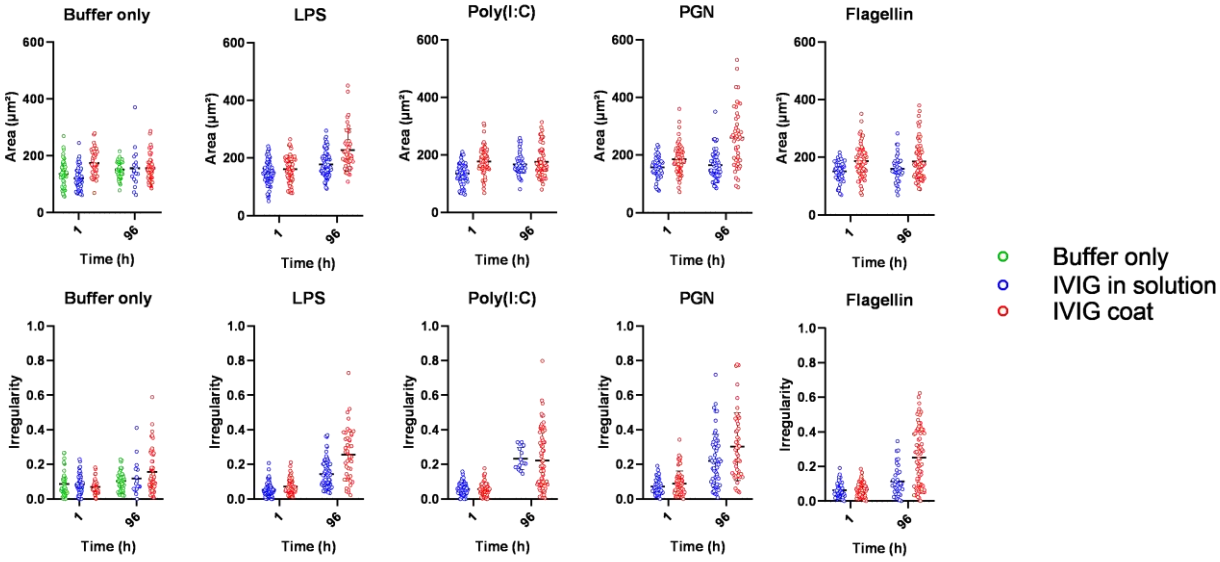

Figure 10. Long term effect of TLR ligands on THP-1 characteristics. *Area and irregularity of THP-1 cells after 1 and 96 hours of incubation, with or without IVIG coat. TLR ligands lipopolysaccharide (LPS), Polyinosinic:polycytidylic acid (Poly(I:C)), peptidoglycan (PGN) and bacterial flagellin were tested as solution. Markers represent single cells.*

Single cell dynamic mass redistribution (DMR) during cell activation

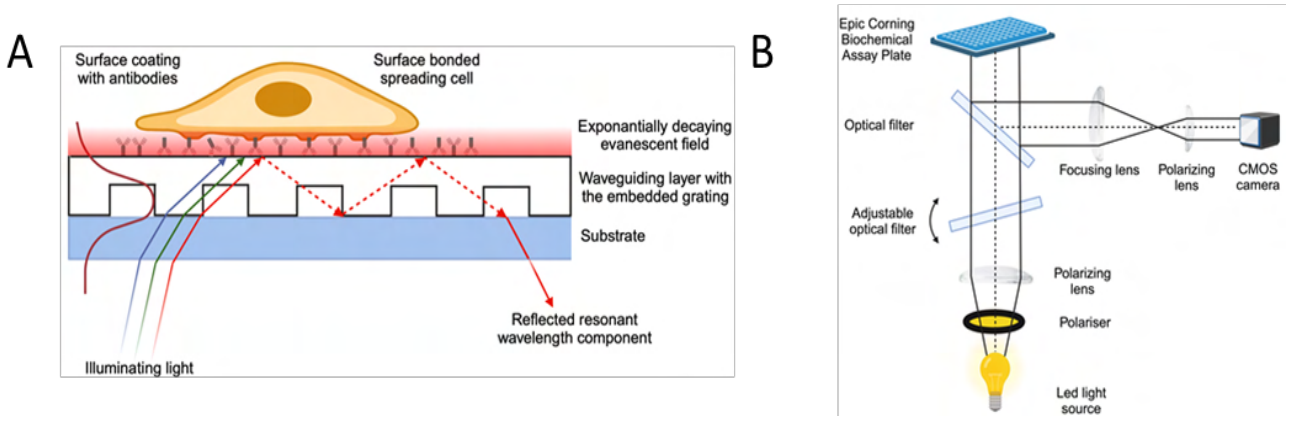

Figure 11. Resonant waveguide grating optical biosensor. A *Working principle and* ***B*** *optical setup of the instrument.*

RWG based biosensors EPIC BT and EPIC Cardio were used to study the changes of the dynamic mass redistribution (DMR) during cell activation. Here, cell activation on the sensor surface results local changes in the refractive index in the evanescent field that will change the light propagating properties of the waveguide resulting a shift in the reflected resonant wavelength component (Fig11).

From our initial measurements we saw that the THP-1 cells bind to the immunoglobulin coated wells, and basically no binding can be seen in the BSA coated well (Fig12A). We also found that the wavelength shift measured is a function of the number of cells in each well. It is important to note that at ~4000 cells per well, no cell adhesion signal can be measured anymore (Fig12A-C), while for our single cell measurements with the higher resolution we used a maximum of 1000 cells per well to minimize the cell density in order to capture as many single cell events as possible (Fig15F).

To show that the interaction is specific we added soluble immunoglobulin into the cell assay buffer, and as expected, at high concentration we could reduce cell adhesion almost completely (Fig12D). Similarly, we checked the optimal FCS content in RPMI based buffers and BSA content in PBS buffers, and found that 10 (%V/V) FCS and 1-0.2 µg/ml provides the most differentiating power between IVIG coated and non-coated surfaces.

While the adaptation of population level, measurements from the lower resolution RWG platform, EPIC BT, proved successful, we matched the cells measured on the sensor surface with those on the micrographs of the same well after fixing the cells (Fig12A-B). However, the handling of single cell data raised an unexpected challenge. Unlike adherent cells, THP-1 cells and leukocytes doesn't necessarily remain active on the sensor surface until the end of the measurement (Fig13C, E), therefore a new evaluation algorithm was developed.

Detection of cell activation and counting The Epic Cardio biosensor exports a video matrix of the concatenated wells with (T, 80 * H, 80 * W) dimensions where T denotes the temporal measurement points, whilst H, W are the height and width arrangement grid of the wells on the microplate. These are separated into individual (N, T, 80, 80) wells, where N = H * W and the wells are preprocessed. The sample is cut to the starting point of the adhesion phase and afterwards two error components are removed from the data. The first is the bias which is removed by subtracting the base wavelength at the initial point of the activation phase.

Afterwards, global background correction is performed, where the mean value of a selected number of background pixels is subtracted from the data to correct for the error caused by for example the

different temperature and consistency of the added buffer solution, or similar sensor drifting phenomena. This is an automated process in which pixel selection happens using a foreground mask. The mask represents active regions on the biosensor surface where the wavelength shifts reaches at least the value of a parameterized constant, in our case 25 pm. Afterwards the selection happens based on three criteria: the randomly selected background pixels have to avoid active mask regions, previously selected pixels and the edge of the biosensor image, where the biosensor can intersect well edges, producing false results. The selected pixels are manually checked to ensure true background selection and afterwards the mean or median signal of the selected pixels is subtracted from the whole well matrix (Fig13D), depending on which results in a clearer sample. Throughout the measurement, the wavelength shift signals associated with a given pixel describe the activation kinetics specific to that cell. After the drift correction, cells are localized using bounded peak local maxima search with manually parametrized minimum and maximum threshold, in our case 25 and 3000 pm values. Cell centers are selected based on the local maxima points of the thresholded mask filtered by a parametrized neighboring radius. This is necessary because it is possible that a single cell may appear on a pixel boundary or the cell surface can produce multiple peaks in close vicinity. These would lead to multiple selections without an adequately selected neighborhood size.

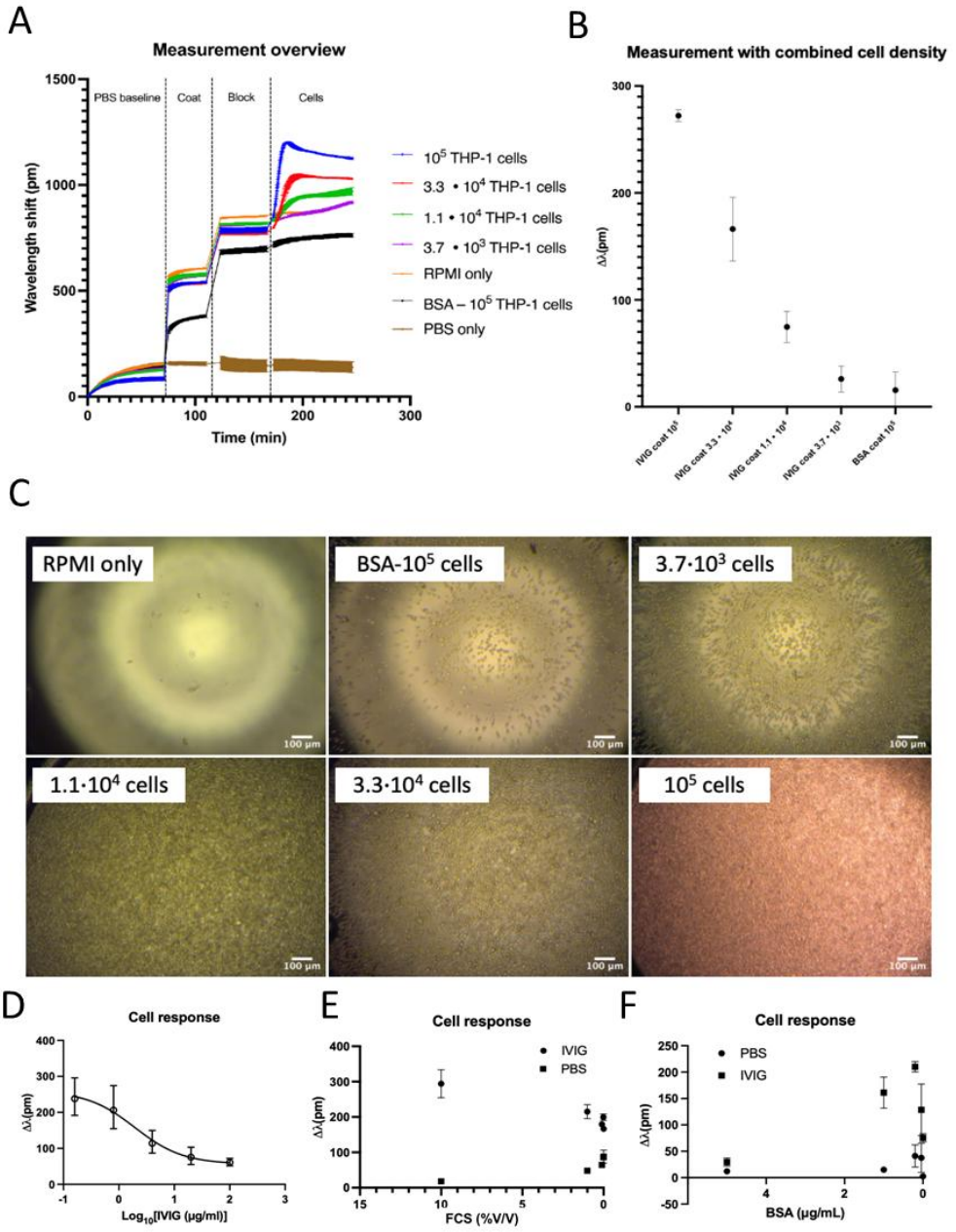

Figure 12. Immunoglobulin triggered activation of THP-1 cells, bulk measurement with EPIC BT*. **A** Overview of the measurement after stabilizing the measurement baseline with PBS buffer, the sensor surface was coated with BSA or IVIG. This was followed by a blocking step, before the addition of cells. In this example the effect of cell numbers was tested. **B** Changes in Wavelength shift compared to baseline values, before the addition of the cells was calculated to evaluate the measurement (n=3). The wavelength shift jump from the cellular baseline after the blocking phase showing the effect of surface treatments on cell activation. **C** Microscope images taken under the different conditions after fixing the cells (Axio Zeiss Observer Z1 microscope, 10 X magnification). **D** The inhibitory effect of soluble IVIG when added to the cell assay buffer. **E** The effect of FCS content in RPMI and **F** BSA concentration in BSA PBS based buffer during cell activation testing.*

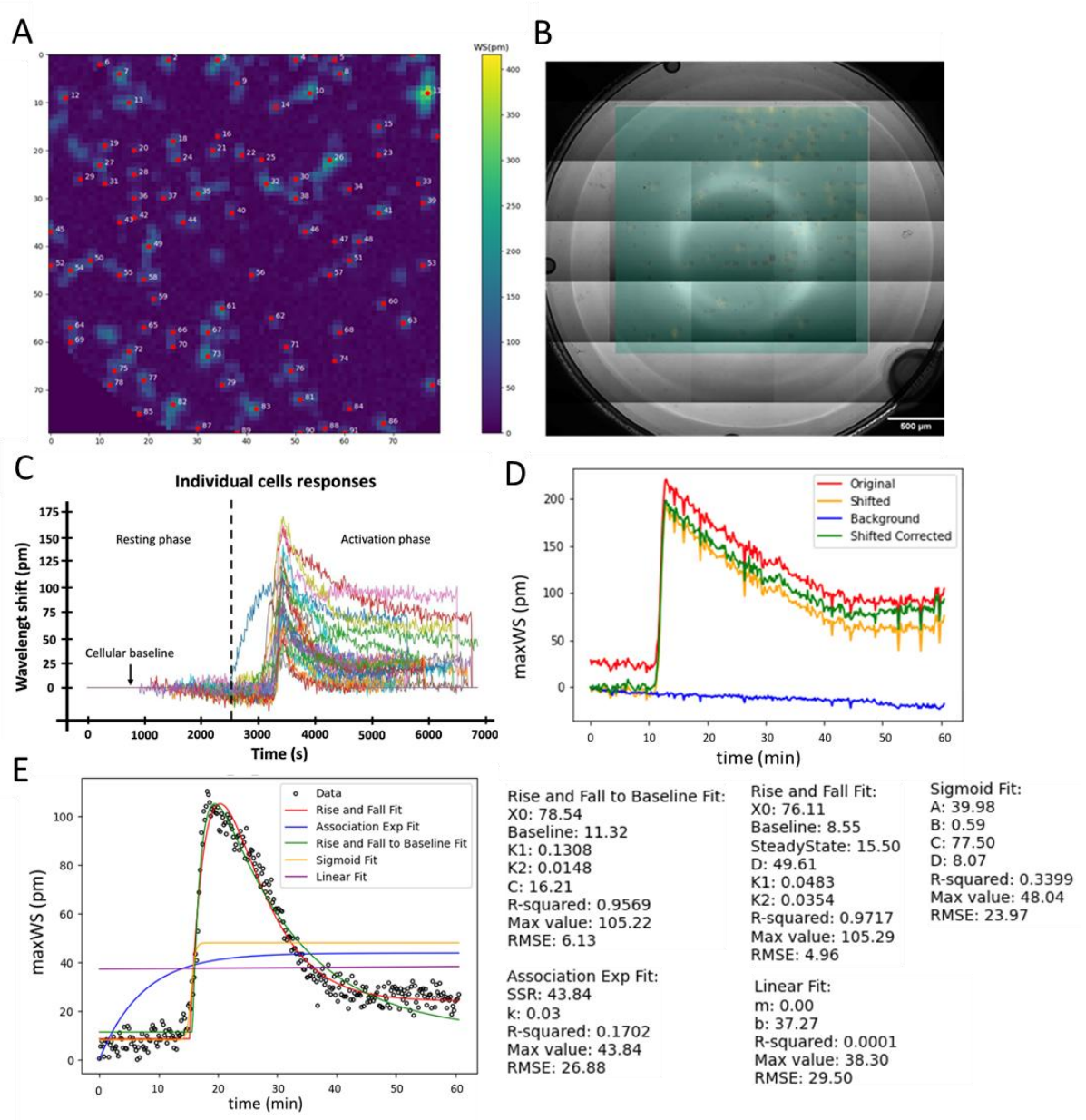

Figure 13. Detection of the activation of individual THP-1 cells with EPIC Cardio single cell resolution biosensor. ***A*** *Sensor image at the end of the measurement, pixels are shown x and y axis. Individual cells are marked with red dots and numbers, while color coding indicates the wavelength shift measured on the given pixels.* ***B*** *RWG sensor image overlapped with micrograph of the microwells containing the sensor for precise localization of the cells for further analysis.* ***C*** *Wavelength shift values of individual cells as a function of time extracted from the measurement frames.* ***D*** *Processing overview of the kinetic activation data curves obtained after background correction and filtering of the wavelength shift data set and the original wavelength shift.* ***E*** *Single cell derived kinetic data fitted with equations describing various time course profiles(Hoare et al., 2020).*

To identify the optimal parameters of signal threshold and neighborhood size, biosensor data was manually compared to the micrographs of the same wells (Fig14). Here, accuracy was calculated as the ratio:

$$A = \frac{TP + TN}{TP + TN + FP + FN}$$

True positive refers to those wavelength shift phenomena that are analyzed based on the shift characteristics of single cells in the image, which are fitted to the microscopic image. These signals correspond to lateral inhomogeneous signals representing activation kinetics, with pixel maximums visible on the biosensor image. True negative includes cells visible on microscopic images and counted by the Cellpose program but not activated. As no wavelength shift phenomenon can be assigned to these cells during analysis with the Cardio evaluator, this category can be calculated as the difference between the total number of cells counted by Cellpose and the total signals detected by the Cardio evaluator, minus the false negatives: Cellpose - (Sum Cardio signal + False negative). False positive signals occur when multiple cells are present in a given pixel, making them unclassifiable as a single cell. This category also includes signals that, although corresponding to single cells, are falsely identified as excess signals from specific activation zones due to a low neighborhood size parameter. Additionally, it includes cases where wavelength shift phenomena are detected in areas where no cells are present, resulting in false recognition. False negative refers to activation regions in the biosensor images where cells are detected at the smallest neighborhood size and lowest threshold values but not at the evaluation setting parameters. To accurately analyze false negatives, it is helpful to examine a single matched image, as some regions may show activation staining at low thresholds where cells are visible in the microscopic image.

A)

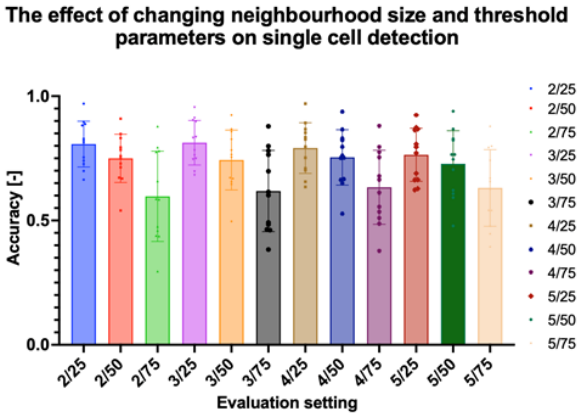

B)

Nighbourhood size/threshold	Accuracy	SD	N
2/25	0.621	0.094	12
2/50	0.712	0.082	12
2/75	0.838	0.047	12
3/25	0.920	0.035	12
3/50	0.630	0.104	12
3/75	0.614	0.126	12
4/25	0.744	0.089	12
4/50	0.826	0.054	12
4/75	0.618	0.108	12
5/25	0.515	0.138	12
5/50	0.837	0.043	12
5/75	0.754	0.064	12

Figure 14. Selection of optimization parameters for single cells RWG evaluation. ***A*** *Diagram showing the optimization of the neighborhood size and wavelength shift threshold limits of the evaluation program, with the tested neighborhood size distances: 2, 3, 4, 5 pixels. The tested wavelength shift threshold limits were 25, 50 and 75 pm.* ***B*** *A summary of the accuracy results is shown in the table, with the best setting highlighted in red.*

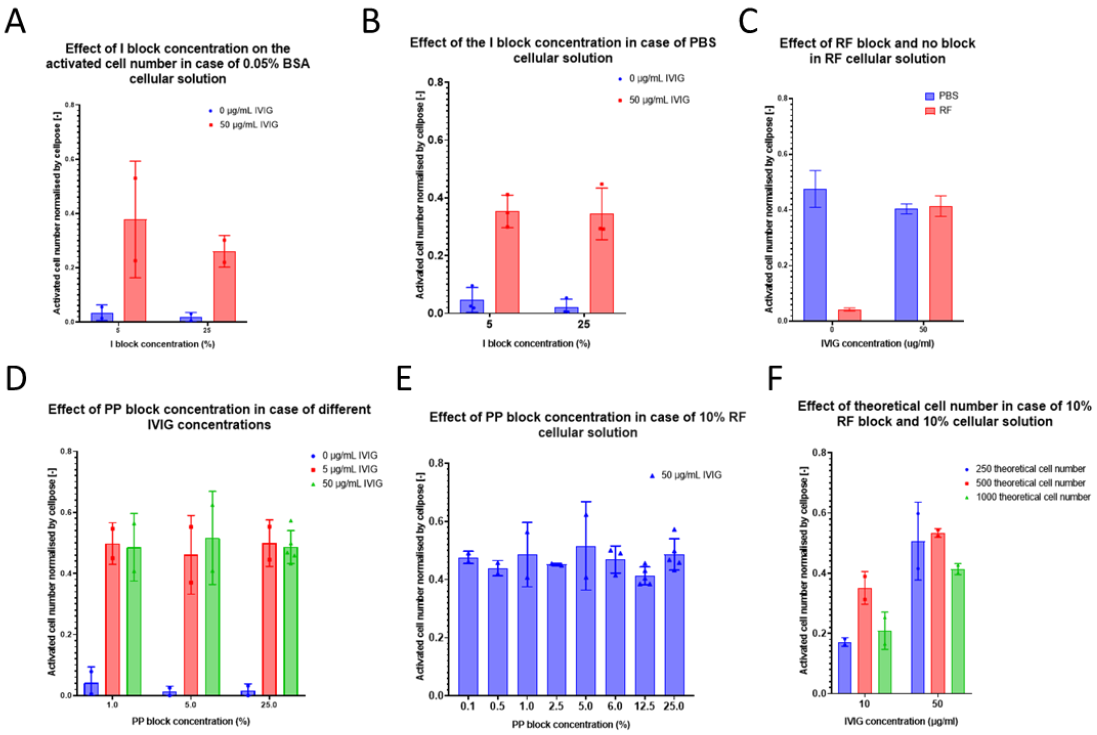

Figure 15. Effect of the blocking strategies used on ratio of THP-1 cells activated. ***A*** *Effect of I-block on activated cell number in cellular solution containing 0.05% BSA, with and without IVIG surface functionalization.* ***B*** *Effect of I-block on activated cell number in on the sensor surface in PBS cellular solution, with and without IVIG surface functionalization.* ***C*** *Ratio of cells activated on RF blocked or non-blocked (PBS) sensor surface with and without IVIG surface functionalization* ***D*** *Ratio of cells activated on PLL-g-PEG blocked sensor surface with and without IVIG surface functionalization.* ***E*** *The effect of changing the concentration of PLL-g-PEG solution used for blocking on the activated cell.* ***F*** *Effect of theoretical cell number on the efficiency of cell activation IVIG functionalized sensor surface.*

Based on the parameters identified for accuracy, we analyzed the effect of blocking solutions on the relative number of activated cells per well on an IVIG-coated surface (Fig15). We found that multiple blocking solutions can be applied, including I-block (Fig15A-B), RPMI + 10% FCS (RF) (Fig15C), and PLL-g-PEG (Fig15D-E), all of which effectively block non-specific cell activation. However, it is important to note that the kinetic profile of cell activation (Fig13E) is also influenced by the blocking solution used. Before testing antigen-bound antibodies, we tested whether TLR ligands could trigger similar cell activation as seen with the IVIG coat. In a one-hour measurement with both THP-1 cells and peripheral blood-derived leukocytes, we observed minimal activation from the ligands alone compared to the activation on the IVIG coat (Fig16). However, we are still investigating whether TLR ligands affect the kinetic profile of activation on the IVIG coat. To test antigen-bound antibodies, we coupled biotinylated rheumatoid arthritis (RA) diagnostic peptides to neutravidin on the sensor surface. After serum treatment (with sera previously analyzed in ELISA), we probed the immune complexes generated on the sensor with THP-1 and blood-derived leukocytes (Fig17). As shown in Figure 18, incubation of the citrullinated 741 CSX multiepitope peptide(Szarka et al., 2018) with positive serum triggered the most pronounced leukocyte activation (Fig18A,E), compared to the treatment with a negative serum sample (Fig18C,E) or the reaction of either serum with the arginine-containing form of the peptide (Fig18B,D).

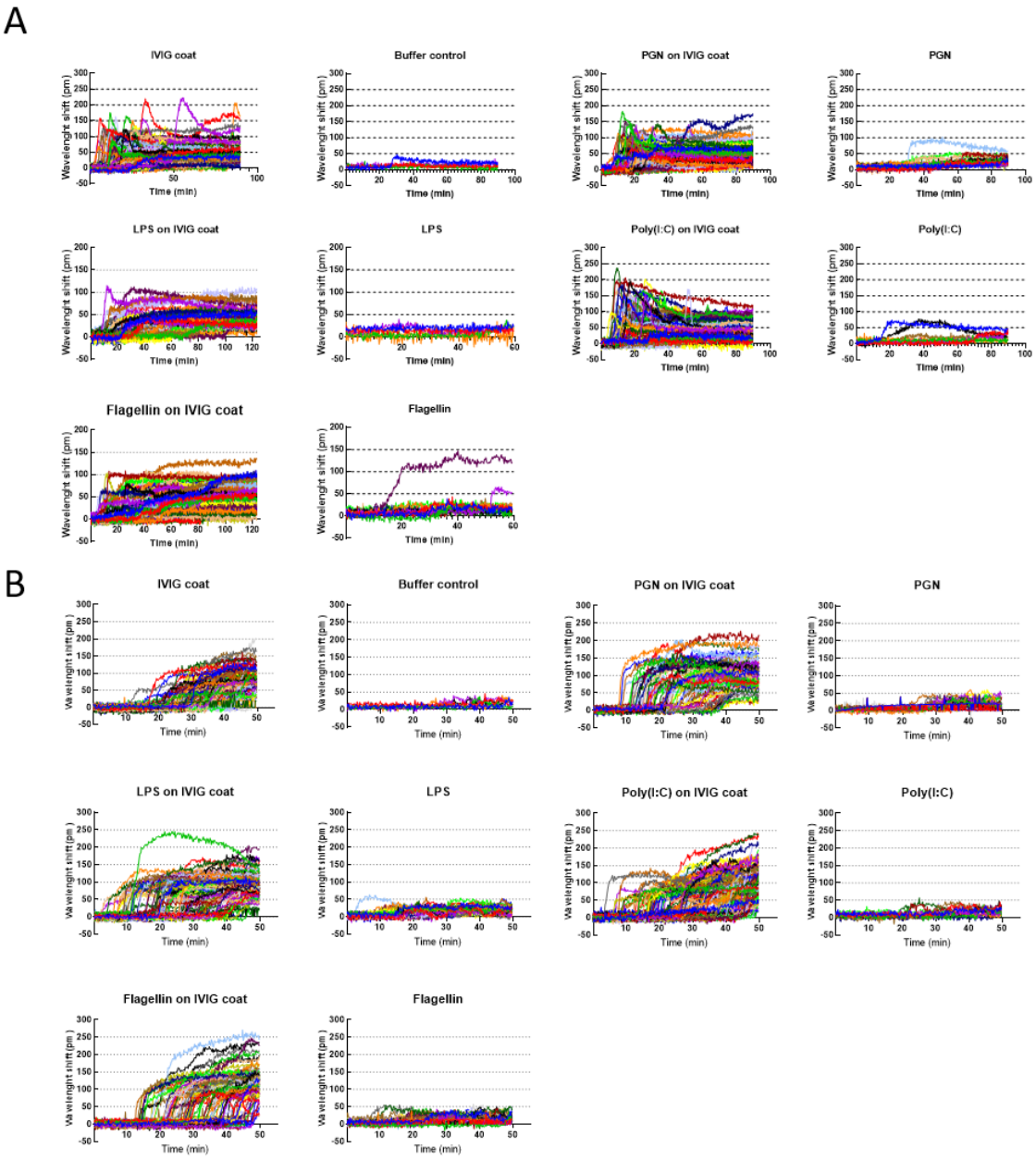

Figure 16. Cell activation in the presence of TLR ligands. The activation of THP-1 cells (A) and peripheral blood derived Leukocytes *(B) were tested in the presence in TLR ligands TLR ligands lipopolysaccharide (LPS), Polyinosinic:polycytidylic acid (Poly(I:C)), peptidoglycan (PGN) and bacterial flagellin were tested in solution, with and without IVIG coat on the sensor surface.*

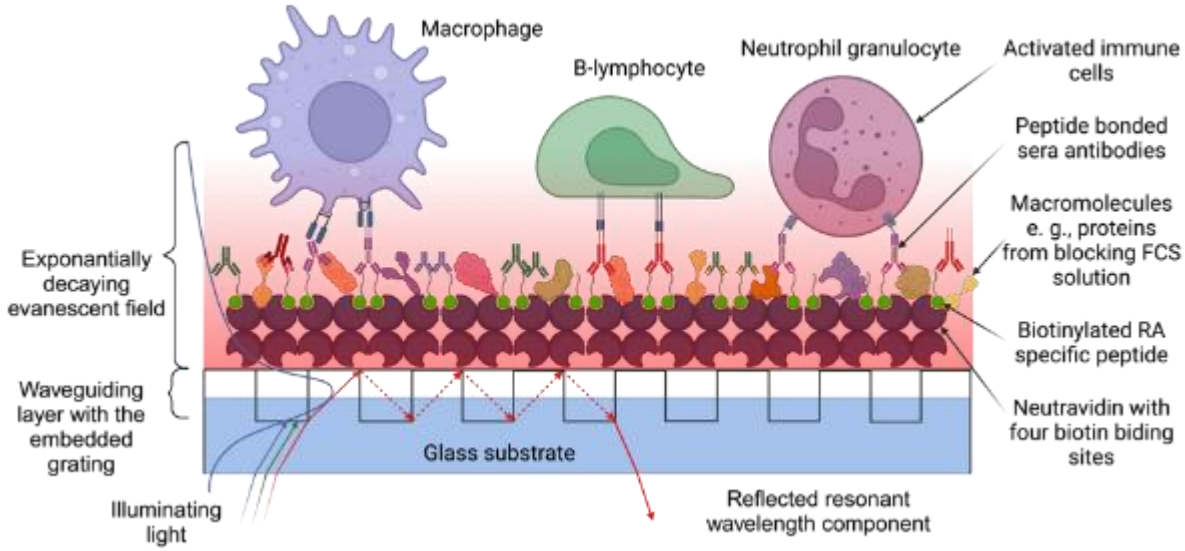

Figure 17. *Overview of the application of the Rheumatoid Arthritis (RA) diagnostic peptide to probe serum reactivity and the following activation of peripheral blood derived leukocytes.*

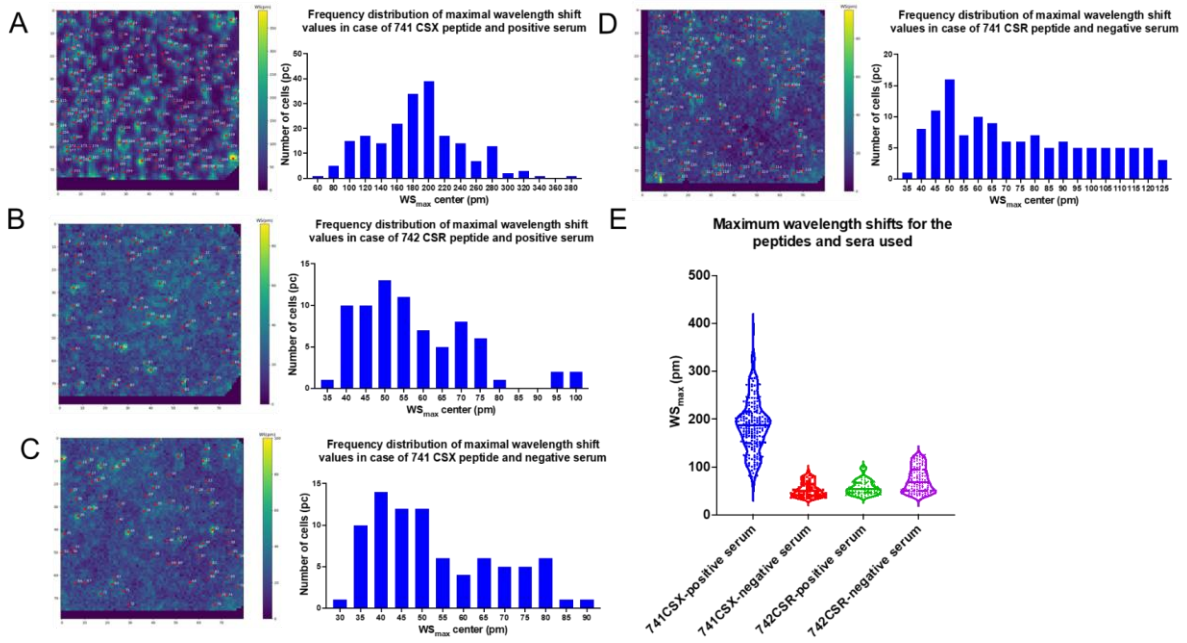

Figure 18. Summary of leukocyte activation after sensor surface functionalization by the formation of immune complexes. *Sensor heat maps of lateral inhomogeneous wavelength shift phenomena, where each red marker indicates the activation zone associated with each surface adhered leukocyte on a functionalized surface of an immune complex with* ***A*** *741 CSX multiepitope peptide and RA positive serum;* ***B*** *742 CSR multiepitope peptide and RA positive serum* ***C*** *741 CSX multiepitope peptide and negative RA serum and* ***D*** *742 CSR multiepitope peptide and RA negative serum and their corresponding frequency distributions of maximal wavelength shift signals associated with leukocyte activation.* ***E*** *Summary of maximum wavelength shifts associated with leukocyte activation for each immune complex treated surface.*

Cell identification

To identify leukocyte subpopulations from peripheral blood on the sensor surface a workflow to fix the cells directly after the measurement was developed in order to match each cell with their measured signals. A protocol that enables fluorescent staining followed by hematological staining was developed. With this we can identify monocytes (Fig19), B-cells(Fig20), T-cells(Fig21) and granulocytes(Fig22) on the sensor surface. Moreover, EPIC Cardio compatible protocols for histological stains (Janus Green, Acridine Orange, Oil Red O, Sudan Black and Nile Blue A) were also developed to gain further insight into potential differentiating factors.

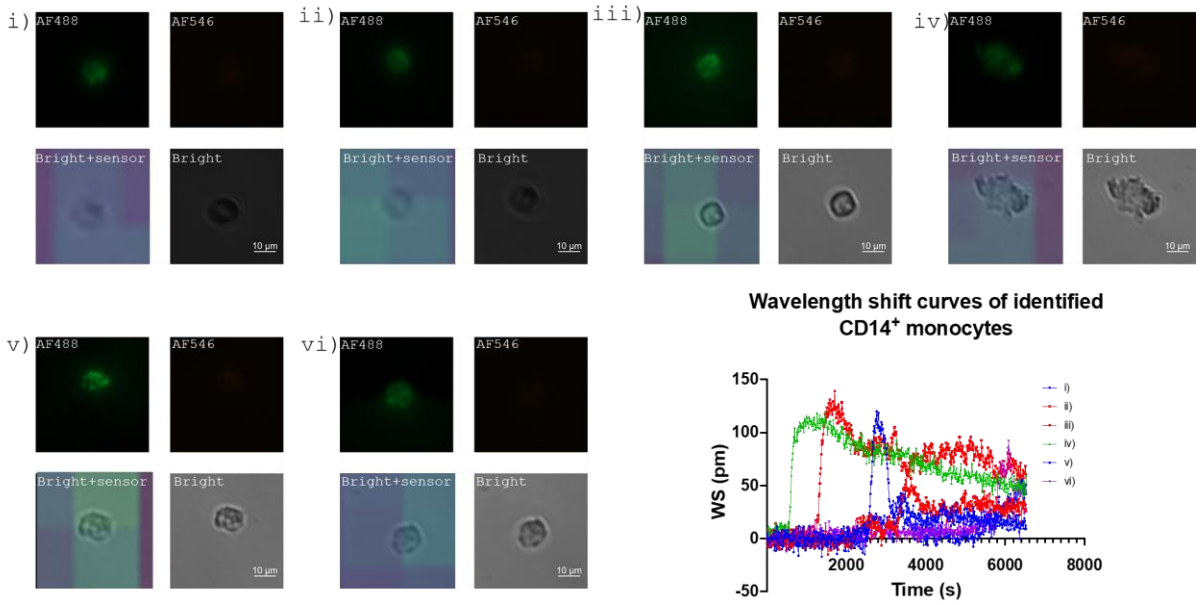

Figure 19. Identification of monocytes on IVIG functionalized sensor surface. *i)-vi) The observed phase contrast microscopic images in 38 HE filter set (ex.: BP 470/40 nm, em.: BP 525/50 nm), 43 HE filter set (ex.: BP 545/25 nm, em.: BP 605/70 nm), brightfield picture and the brightfield picture fitted with the sensor image. Cells were fixed with 4% PFA solution (diluted with 1x DPBS), blocked with 5% BSA solution and labelled 2.47 µg/mL anti-CD14-Alexa 488 (clone: 5A3B11B5) (Santa Cruz) monoclonal antibody solution diluted 1:80 with 1% BSA solution for 2 hours. The identified monocyte activation wavelength shift curves re shown as well.*

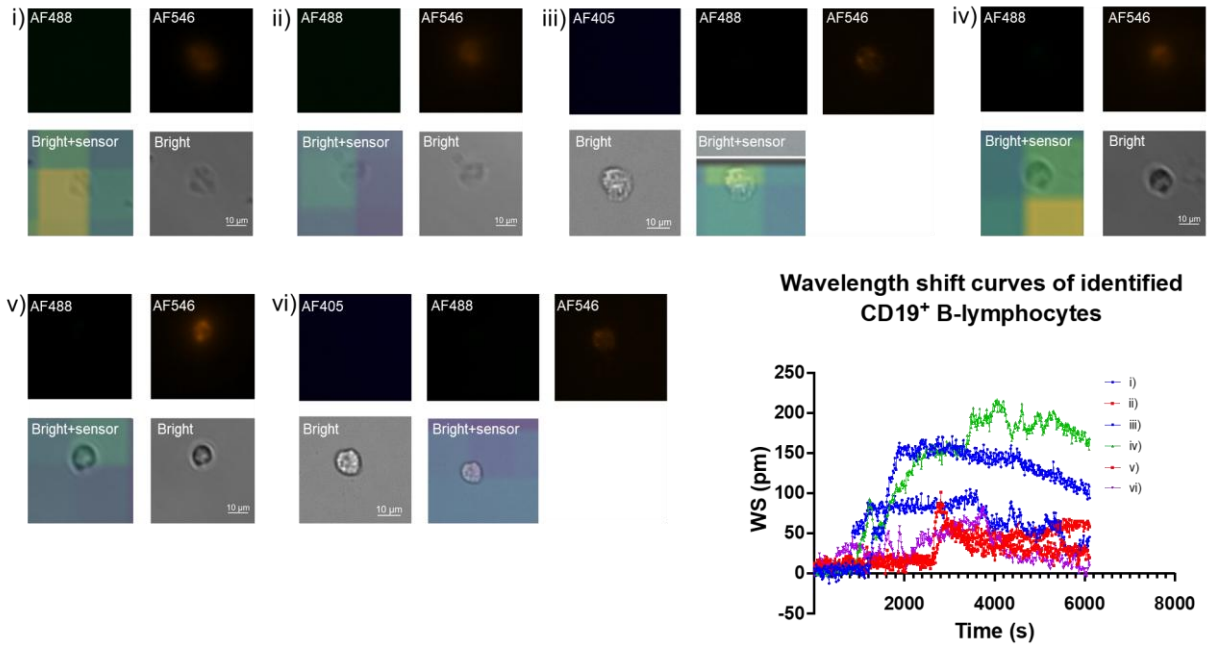

Figure 20. Identification of B-lymphocytes on IVIG functionalized sensor surface. *i)-vi) The observed phase contrast microscopic images in 43 HE filter set (ex.: BP 470/40 nm, em.: BP 525/50 nm), 43 HE filter set (ex.: BP 545/25 nm, em.: BP 605/70 nm), brightfield picture and the brightfield picture fitted with the sensor image. Cells were fixed with 4% PFA solution (diluted with 1x DPBS), blocked with 5% BSA solution and labelled 2.47 µg/mL anti-CD19-Alexa 546 (clone: F-3) (Santa Cruz) monoclonal antibody solution diluted 1:80 with 1% BSA solution for 2 hours. The identified B-cell activation wavelength shift curves are shown as well.*

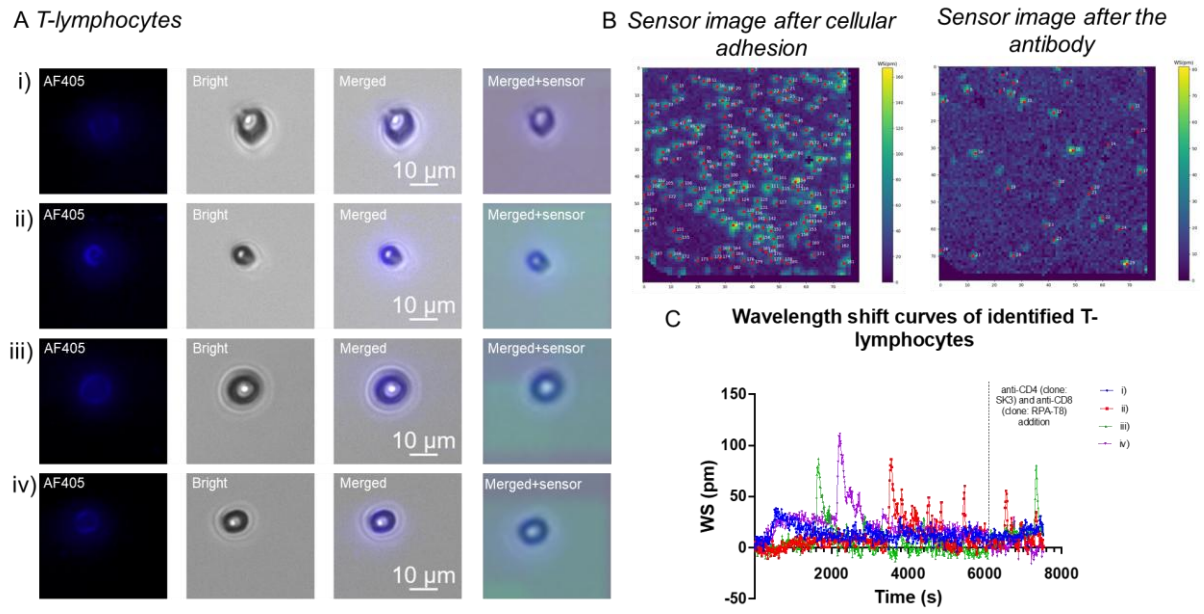

Figure 21. Overview of the T-lymphocyte screening. ***A*** *i-vi) Results of labelling with anti-CD3-Alexa 405 (clone PC3/188A) (Santa Cruz) monoclonal antibody solution diluted 1:20 with 2% BSA solution (fixation with 4% PFA solution, blocking with 2% BSA solution) using fluorescent filter set 2 (ex: G 365 nm, em: LP 420 nm).* ***B*** *Inhomogeneous lateral sensory heat maps of T lymphocyte adhesion on a surface functionalized with 10 µg/mL anti-CD3 (clone: SK7) monoclonal antibody solution and the phenomena observed after cell adhesion with labelling with additional anti-CD4 (clone: SK3) and anti-CD8 (RPA-*

T8) monoclonal antibodies. ***C*** *Curves characterizing the activation of T lymphocytes stained with fluorescently conjugated monoclonal antibody solution and curve segments indicating the binding of secondary antibodies.*

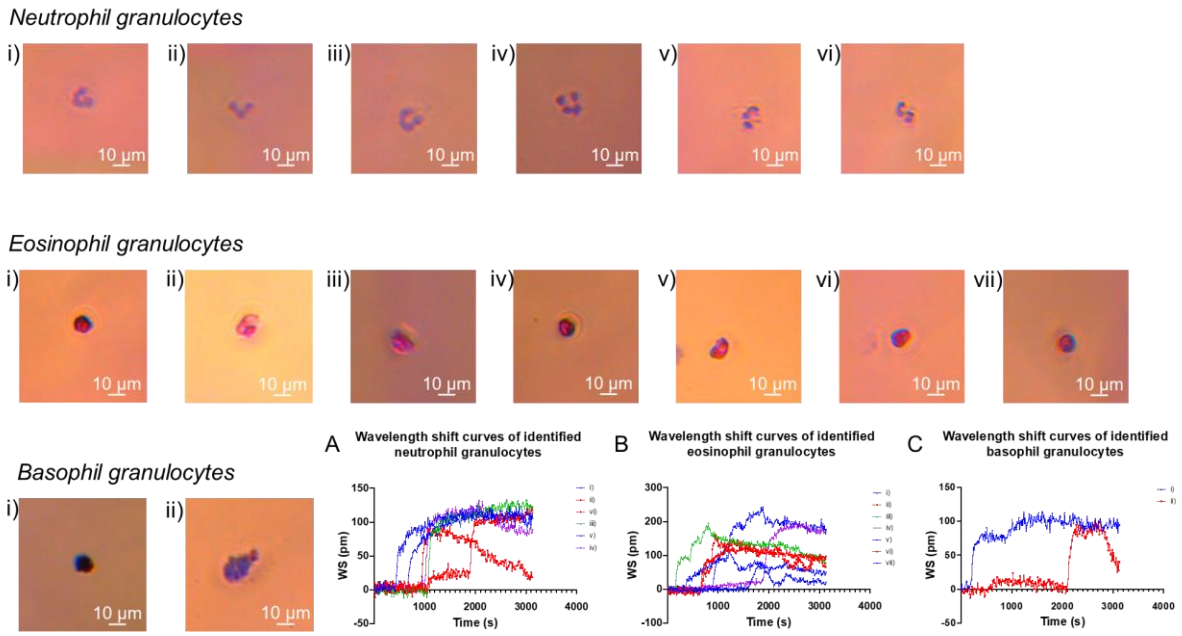

Figure 22. Identification of granulocytes on RWG biosensors. *Color brightfield phase contrast microscopy image of neutrophil (i-vi), eosinophil (i-vii) and basophil (i-ii) granulocytes identified by Wright-Giemsa hematological staining (20x objective, AxioCam ERc 5s).* ***A*** *Activation wavelength shift curves assigned to neutrophil granulocytes identified by staining on a 100 µg/mL IVIG functionalized sensor surface.* ***B*** *Activation wavelength shift curves assigned to eosinophil granulocytes identified by staining on a 100 µg/mL IVIG functionalized sensor surface.* ***C*** *Activation wavelength shift curves assigned to basophil granulocytes identified by staining on a 100 µg/mL IVIG functionalized sensor surface.*

Analysis process for clustering and shapelet distance-based analysis of time series data

To discover subpopulations in the measured data in an unbiased manner, we performed a time series analysis using shapelet extraction and clustering. To achieve this, a multi-step data processing and clustering workflow was developed during the analysis process.

At the beginning of the evaluation process, the data undergoes a preprocessing stage, where each time series is scaled to the interval (0,1) using MinMax normalization. After that, feature extraction is performed, where the signals are partitioned into an adjustable number of subsequences. These represent local patterns in the data (shapelets), which can be used to differentiate subpopulations by their characteristic underlying processes. After the signals are partitioned their subsequences are gathered into a joint shapelet matrix.

After the shapelets are extracted, the shapelet-to-complete signal distances are calculated. The distances can be used to discover cluster-specific patterns since different signals, where cells undergo the same activation subprocess, will provide similar shapelets for the subprocess which results in lower distance values. This suggests that the shape distance data can be used to divide the signals into clusters. During the distance calculation, cell signals are compared to every shapelet in the matrix. The comparison is achieved by selecting the subsequences corresponding to a cell from the shapelet matrix and comparing it to all the subsequences in the matrix. We used Euclidean distance for distance

calculation. This process can be tested later with additional distance metrics (e.g. absolute, Minkowski, Canberra distance or Dynamic Time Warping).

We then organized the distance data into a matrix form and performed signal clustering using the KMeans method. For this, we used the TimeSeriesKMeans algorithm from the TSLearn Python library, which is specifically optimized for time series data and can take local patterns into account through its shape distance-based approach.

Since, in our case the number of subpopulations is unknown, we optimized the window ratio and cluster numbers using different clustering metrics. (The window ratio is given by the number of subsequences a signal is partitioned into.) For this, we chose the Silhouette score, the Calinski-Harabasz index, and the Davies-Bouldin index as metrics. The Silhouette score measures the ratio of the distance within each cluster to the distance between clusters, while the Calinski-Harabasz index analyzes the ratio of the variance between clusters, and the Davies-Bouldin index examines the ratio of the average distance between each cluster.

To optimize the method, we used a grid search, during which the evaluation is run for every input variable combination. The optimization results in a separate vector for all metric values. Afterwards the optimal setting for the process is evaluated by finding the global optimum point in these vectors.

For the clustering process, we combined data from 5 measurements, which contained more than 5000 single-cell signals. During the optimization, we examined the efficiency of the clustering process as a function of the number of shapelets and the number of clusters. The window ratio was given by dividing the signal into N parts where $N \in [3, 5,10,20,30,40,50]$, and the cluster number K was given by dividing it into $K \in [3,4,5,6,7,8]$ clusters.

The results of the optimization process are illustrated in Figure 23. From the perspective of the interpretation of the metrics, for Silhouette score and Calinski-Harabasz index the maximum values, and for the Davies-Bouldin index the minimum value indicate optimal clustering. Knowing these and based on Figures 2, it can be concluded that the values 4-5 indicate the optimal value for the cluster number, since in this interval all metrics are in the optimal region. Based on Figure 1, a local minimum valley is found in the parameter diagonal for the Davies-Bouldin index, which takes the global minimum between the values 20-30. Similarly, a local maximum line can be found in the case of the Silhouette score and the Calinski-Harabasz index, which decreases towards the lower sequence number. These metrics assume an optimum value between 30-40, which suggests that the optimal value would between the 20-40 interval. While these results show our data processing approach successfully cluster similar activation patterns together (Fig23B-C), parameters and processing algorithm strategies are to be further optimized and explored. Furthermore, to match the clusters with phenotypic data we are currently optimizing the data evaluation pipeline to automatically match the data from 4 fluorescent and the color brightfield phase contrast microscopy channels to provide to complete the analysis. We filed a provisional patent on the classification and profiling of single cells based on their kinetic activation profile in optical biosensor measurements.

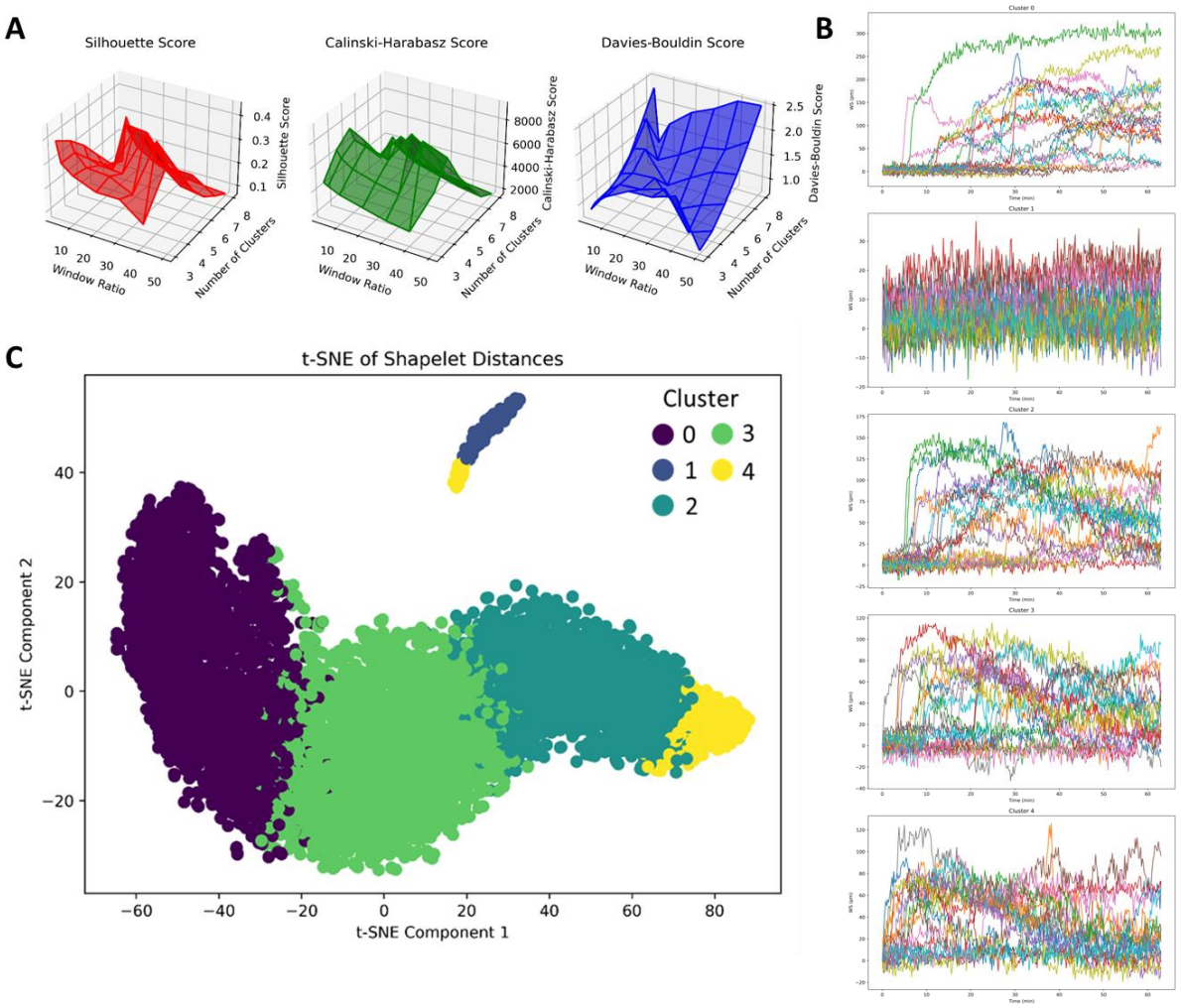

Figure 23. Shapelet based clustering of RWG based leukocyte activation signals. A *Shows the grid optimization metric values as a function of the window ratio, the number of segments the total activation signal partitioned into, and the number of clusters. Window Ratio indicates the subsequence rate, here window ratio of 20 was used with a cluster number of 5 in (B) and (C). B t-distributed stochastic neighbor embedding representation of the clustering based on shapelet occurrences. C Representative single cells activation kinetics in each cluster.*

Summary

We determined various biophysical parameters during immunoglobulin-triggered activation of THP-1 monocytes and leukocytes. Our findings revealed that while tools like CCMP and FluidFM, along with the Holomonitor, are useful for long-term measurements (e.g., to follow cell differentiation), they have significant disadvantages. Specifically, the signal-to-noise ratio achieved with these tools is not optimal, and while motility and cell area can be measured, they may not fully capture the complexity of the activation process.

Data from RWG-based single-cell measurements indicated that cell activity and interaction with the surface constantly change during activation. This explains the considerable variation observed in adhesion force-based measurements and highlights the importance of real-time monitoring of cell activation.

In CCMP-based measurements, we showed that activation occurs only in viable cells. We also tested the differences between IgG- and TLR ligand-triggered activation and found that they are distinguishable. Without the immunoglobulin coat, cells do not activate on the biosensor. This finding

allows for the testing of antigens with various chemical compositions, as cells did not activate under the conditions tested. For functional serology, RWG-based measurements are the most useful because they allow us to: 1) follow single-cell activation kinetics in real time; 2) reliably fix and stain single cells; and 3) measure single cells in 12 separate wells with remarkable time resolution.

We also tested cell activation on immune complexes generated on the sensor using rheumatoid arthritis-specific diagnostic peptides. In the presence of antigen-specific antibodies, the immune complexes triggered cell activation similar to the IgG-triggered activation observed with citrulline-containing peptides. To investigate the activation signals of leukocytes, we applied two different staining procedures. First, classical hematological stains identified single cells, which were useful for identifying granulocyte subpopulations. We also used fluorescent dye-conjugated lineage-specific antibodies to identify lymphocyte subpopulations.

For THP-1 cells, activation kinetics followed predictable patterns, including rise-and-fall dynamics to either baseline or steady-state levels. In contrast, primary leukocytes exhibited more diverse activation kinetics, requiring clustering-based approaches to identify activation subtypes. Preliminary tests with TLR ligands and complement activation on the sensor surface emphasized the complexity of leukocyte activation, underlining the need for refining single-cell resolution methods to capture subgroup-specific activation characteristics. By integrating advanced biophysical techniques with robust data processing workflows, we demonstrated the potential of optical biosensors to provide high-resolution, information-dense data for studying leukocyte activation. This approach could be invaluable for profiling humoral immune response antibody effector functions in personalized fashion, aiding in the study of infectious and autoimmune diseases, and assessing the efficacy of immunotherapeutic reagents.

Seven MSc students successfully defended their theses under our shared supervision with Róbert Horváth. Bence Joó worked on the initial setup of blocking and buffer testing in the EPIC Cardio and Holomonitor systems. Tamás Hajdu investigated the correlation between Cardio and CCMP and established a measurement protocol. Szabolcs Novák worked on the comparison of CCMP and FluidFM, while Igor Sallai worked on the EPIC Cardio measurements and the development of cell fixing and staining procedures. Dávid Visnyei studied polyacrylamide gels and examined cell activation on these surfaces. Péter Joó studied the short- and long-term effects of TLR ligands. Zsolt Janka worked on immune complex generation for EPIC Cardio and Holomonitor techniques. Bálint Béres and his students worked on the development of the data processing platform. Péter Joó, Igor Sallai, and Szabolcs Novák are currently PhD students in our laboratory.

References

Altschuler, S.J., Wu, L.F., 2010. Cellular Heterogeneity: Do Differences Make a Difference? Cell 141, 559–563. https://doi.org/10.1016/j.cell.2010.04.033

Bányász, I., Rajta, I., Havránek, V., Mackova, A., Laki, A.J., Kellermayer, M.S.Z., Szittner, Z., Kurunczi, S., Novák, Sz., Székács, I., Horváth, R., Fried, M., Nagy, G.U.L., 2023. Design, fabrication, and characterization of picowell arrays on cyclic olefin copolymer surfaces generated with a 10.5 MeV N4+ ion microbeam. Applied Physics Letters 123, 053701. https://doi.org/10.1063/5.0155681

Hoare, S.R.J., Tewson, P.H., Quinn, A.M., Hughes, T.E., Bridge, L.J., 2020. Analyzing kinetic signaling data for G-protein-coupled receptors. Sci Rep 10, 12263. https://doi.org/10.1038/s41598-020-67844-3

Lodge, J., Kajtar, L., Duxbury, R., Hall, D., Burley, G.A., Cordy, J., Yates, J.W.T., Rattray, Z., 2025. Quantifying antibody binding: techniques and therapeutic implications. mAbs 17, 2459795. https://doi.org/10.1080/19420862.2025.2459795

Loos, C., Coccia, M., Didierlaurent, A.M., Essaghir, A., Fallon, J.K., Lauffenburger, D., Luedemann, C., Michell, A., van der Most, R., Zhu, A.L., Alter, G., Burny, W., 2023. Systems serology-based comparison of antibody effector functions induced by adjuvanted vaccines to guide vaccine design. npj Vaccines 8, 1–15. https://doi.org/10.1038/s41541-023-00613-1

Lu, L.L., Suscovich, T.J., Fortune, S.M., Alter, G., 2018. Beyond binding: antibody effector functions in infectious diseases. Nat Rev Immunol 18, 46–61. https://doi.org/10.1038/nri.2017.106

Satija, R., Shalek, A.K., 2014. Heterogeneity in immune responses: from populations to single cells. Trends in Immunology, Gene Expression in the Immune System 35, 219–229. https://doi.org/10.1016/j.it.2014.03.004

Szarka, E., Aradi, P., Huber, K., Pozsgay, J., Végh, L., Magyar, A., Gyulai, G., Nagy, G., Rojkovich, B., Kiss, É., Hudecz, F., Sármay, G., 2018. Affinity Purification and Comparative Biosensor Analysis of Citrulline-Peptide-Specific Antibodies in Rheumatoid Arthritis. IJMS 19, 326. https://doi.org/10.3390/ijms19010326

Szittner, Z., Péter, B., Kurunczi, S., Székács, I., Horvath, R., 2022. Functional blood cell analysis by label-free biosensors and single-cell technologies. Advances in Colloid and Interface Science 308, 102727. https://doi.org/10.1016/j.cis.2022.102727